IEEE Access
Multidisciplinary ⋮ Rapid Review ⋮ Open Access Journal

Received March 15, 2022, accepted March 30, 2022, date of publication April 11, 2022, date of current version April 21, 2022.

Digital Object Identifier 10.1109/ACCESS.2022.3166509

Wide-Angle Ceramic Retroreflective Luneburg Lens Based on Quasi-Conformal Transformation Optics for Mm-Wave Indoor Localization

PETR KADĚRA[1], (Graduate Student Member, IEEE), JESÚS SÁNCHEZ-PASTOR[2], (Graduate Student Member, IEEE), HOSSEIN ESKANDARI[3], TOMÁŠ TYC[4], MASOUD SAKAKI[5], MARTIN SCHÜßLER[2], ROLF JAKOBY[2], (Member, IEEE), NIELS BENSON[5], (Member, IEEE), ALEJANDRO JIMÉNEZ-SÁEZ[2], (Member, IEEE), AND JAROSLAV LÁČÍK[1], (Member, IEEE)

[1]Department of Radio Electronics, Brno University of Technology, 616 00 Brno, Czech Republic
[2]Institute of Microwave Engineering and Photonics, Technische Universität Darmstadt, 64283 Darmstadt, Germany
[3]Department of Electrical Engineering, Ferdowsi University of Mashhad, Mashhad 9177948944, Iran
[4]Faculty of Science, Institute of Theoretical Physics and Astrophysics, Masaryk University, 611 37 Brno, Czech Republic
[5]Institute of Technology for Nanostructures and Technology, Universität Duisburg–Essen, 47057 Duisburg, Germany

Corresponding authors: Petr Kaděra (kadera@vutbr.cz) and Jesús Sánchez-Pastor (jesus.sanchez@tu-darmstadt.de)

This work was funded by the Quality internal grants of Brno University of Technology, project no. CZ.02.2.69/0.0/0.0/19_073/0016948 and the German Research Foundation (''Deutsche Forschungsgemeinschaft'') (DFG) under Project-ID 287022738 TRR 196 for Project C09. We acknowledge the Open Access support provided by Czech Technical Library.

ABSTRACT This paper presents a quasi-conformal transformation optics (QCTO) based three-dimensional (3D) retroreflective flattened Luneburg lens for wide-angle millimeter-wave radio-frequency indoor localization. The maximum detection angle and radar cross-section (RCS) are investigated, including an impedance matching layer (IML) between the lens antenna and the free-space environment. The 3D QCTO Luneburg lenses are fabricated in alumina by lithography-based ceramic manufacturing, a 3D printing process. The manufactured structures have a diameter of 29.9 mm (4 λ_0), showing a maximum realized gain of 16.51 dBi and beam steering angle of $\pm 70°$ at 40 GHz. The proposed QCTO Luneburg lens with a metallic reflective layer achieves a maximum RCS of -20.05 dBsqm at 40 GHz with a wide-angle response over $\pm 37°$, while the structure with an IML between the lens and air improves these values to a maximum RCS of -15.78 dBsqm and operating angular response between $\pm 50°$.

INDEX TERMS Transformation optics, Luneburg lens, impedance matching, lens antenna, retroreflector, ceramic 3D printing, indoor localization, mm-wave, artificial dielectrics, chipless RFID.

I. INTRODUCTION

The area of passive retroreflective devices for mm-wave (30-300 GHz) and THz wave (0.3-10 THz) communication, objects tracking and indoor localization and identification has recently received increased attention [1]–[14]. Retroreflectors are devices that reflect an incoming electromagnetic (EM) wave into the direction of its arrival and serve for radar cross-section (RCS) enhancement, thus increasing detectability of the specified objects, e. g. drones, satellites, or airplanes. Retroreflectors based on different technological realizations in available literature are presented. For example, Van Atta arrays are formed by planar patches [1] or substrate integrated waveguides [2]. Moreover, frequency-coded corner reflectors are achieved by employing frequency selective surfaces [3], [4] or dielectric resonator arrays [5]–[7]. A large number of retroreflective structures are based on lenses by incorporating a reflective layer, such as frequency-coded fused silica spherical lenses [8], [9], or lenses backed by a photonic crystal (PhC)-based structures [10], such as a polyethylene lens with a Bragg grating [11], and planar [12] or spherical [13] gradient-index Luneburg lens backed by planar PhCs. Finally, the Luneburg lens can also be employed to achieve an omnidirectional retroreflector when it is surrounded by slant polarizers [14]. Most of the aforementioned references use frequency coding, enabling their employment

The associate editor coordinating the review of this manuscript and approving it for publication was Rajkishor Kumar.

in different areas. For instance, in chipless indoor self-localization systems [3], the ability to distinguish between retroreflectors inside the building allows for a precise position calculation, which is achieved by incorporating different and distinguishable frequency-coded signatures to the reflected wave of each retroreflector [3]–[13]. The advances in those researches bring unconventional retroreflectors based on metasurfaces [15]–[18], or transformation optics (TO) principles [19]–[23]. A summary of different retroreflectors and their operational angular range is presented in Table 1. However, the metasurfaces and TO-based retroreflectors have been proposed and realized only up to centimeter frequency bands (0.3-30 GHz) or in optics, outside the mm-wave region.

The use of retroreflectors at mm-wave frequencies allows for wider absolute bandwidths, i.e., a better ranging accuracy and smaller devices, as well as higher antenna gains [6]. More details can be found in our previous work [13], where a combination of a spherical 3D Luneburg lens with 2D PhC coding particles is introduced at 80 GHz. Further, in [24], we addressed the current limitations of a lens-based system due to the limited angular response and overall reduced compactness of the coding particles, i.e., having to adapt the employed planar coding particles (2D PhC, resonating element arrays) to the spherical surface of a lens introduces undesired effects. For example, in [4] the curvature of the employed cross-dipole frequency surface decreases frequency selectivity. In addition, in 2D PhC-based coding [12], the curvature of the lens introduces structural distortions that results in a larger required angular separation between coding particles. To answer these challenges, we proposed a theoretical concept of a 3D flattened quasi-conformal transformation optics (QCTO) Luneburg lens backed by a 3D PhC coding structure [24], which showed a large potential for developing integrated wide-angle passive frequency-coded retroreflective devices since the flat bottom of the QCTO lens allows for easier integration of different coding particles. However, the required high permittivity of the lens ($\varepsilon_r = 17.5$) does not allow the usage of the same material as for the PhC coding part ($\varepsilon_r = 9.5$). Therefore, including the manufacturing and integration options enabled by ceramic 3D printing [25], [26], a new design addressing this problem is required.

This paper presents the design and manufacturing of a ceramic wide-angle 3D QCTO Luneburg lens working in the Ka-band, as the first step towards frequency-coded monolithic ceramic-based tags for indoor localization applications. The design incorporates an impedance matching layer (IML) to the air as well. The high permittivity of alumina allows wide coverage angles while ensuring very stable operation in harsh environments (high-temperature, ionizing, chemically polluted) [3]. To the knowledge of the authors, this is the first time that an alumina-based QCTO Luneburg lens antenna with wide 3D operating angular range is presented, and its performance as a retroreflector is evaluated. The paper is organized as follows: Section II presents a study on QCTO Luneburg lenses; their maximum required permittivity and angular range. Section III deals with the manufacturing restrictions, their effects on the lens performance and fabrication process realized by ceramic 3D printing, and the measurement results. In Section IV, the achieved results and future improvements are discussed.

TABLE 1. Comparison of selected retroreflectors and their operational angular range. Retroreflectors in mm-wave region are highlighted in light blue color.

Ref.	Retroreflector type	Operational angle [°]	Freq. coding	Freq. [GHz]
[1]	Van Atta array	± 52*	no	200
[2]	Van Atta array	± 42*	no	78.6
[3]	Cross-dipole FSS + trihedral corner	± 22*	yes	77
[4]	Gridded square-ring FSS + trihedral corner	± 24*	yes	105
[7]	Spherical DR + dihedral corner	± 20	yes	84 100
[8]	Cross-dipole FSS + spherical lens	± 38*	yes	160
[9]	Cross-dipole FSS + spherical lens	± 60*	yes	82
[10] [12]	Cylindrical PhC DR + 2D planar Luneburg lens	± 65	yes	237.7
[13]	Cylindrical PhC DR + 3D spherical Luneburg lens	± 72*	yes	76.5
[14]	Omnidirectional 3D spherical Luneburg lens	± 180*	no	30
[15]	Planar metasurface with metal mirror	± 32*	no	10
[17]	Planar metasurface with helicity-switching	-70 to -40 **	yes	10
[18]	Spin-locked metasurface	10 to 20	no	15
[19]	Optics surface transformation (microchannel planar surface)	± 80”	poten-tially	-
[20]	Omnidirectional transformation optics	± 180	poten-tially	8.9
[22]	Flattened trihedral corner with transformation optics	± 45”	no	8
[23]	Parabolic with Schwarz-Christoffel transformation optics	± 57”	no	5
[24]	3D PhC DR + 3D QCTO Luneburg lens	± 75”	yes	79
This work	**Alumina 3D QCTO Luneburg lens**	**± 50**	**yes**	**40**

* 6 dB drop from its maximum RCS value.
** Frequency-dependent angle of retroreflection.
” Simulated only

II. QUASI-CONFORMAL TRANSFORMATION OPTICS ENABLED LUNEBURG LENS

The transformation optics theory has gained popularity in the last two decades for providing a systematic approach to the design of invisible cloaks [27]–[31], conformal antenna arrays [32], [33], directivity enhancers [34], [35],

and waveguide bends and couplers [36]–[38]. TO has also been employed to modify the geometry of various dielectric lenses [39]–[53].

The transformation optics establishes a relation between the fields and the material between two spaces: the virtual space where the wave propagation properties are known, and the physical space. A spatial deformation is applied to the virtual space to attain a desired behavior for the electromagnetic waves. Using the transformation optics recipe, one can calculate a transformation medium for the physical space that mimics the desired space transformation. The transformation medium is quite complex if the underlying transformations are general. However, employing conformal and quasi-conformal transformations simplifies the derived material and leads to an all-dielectric, isotropic solution [42], [43], [51].

The QCTO has been used to modify the geometry of the Luneburg lens [54], by flattening a portion of the lens contour [40], [44], [50]–[53]. This creates a planar surface suitable for placing a 3D PhC medium with an array of embedded high-Q resonators for frequency coding as proposed in [24]. However, by applying QCTO to the Luneburg lens, the required maximum relative permittivity values increases drastically compared to the conventional Luneburg lens [40], [44], [50]–[53]. This drawback results in a significant impedance mismatch at the boundaries between the modified lens and the surrounding medium (usually free space). Furthermore, this mismatch is amplified if a larger portion of the lens contour is flattened. The solution for this defect was proposed by Biswas *et al.* in [52] where an anti-reflective (AR) layer was added to the flattened area of the QCTO lens resulting in an improved antenna impedance matching and an enhancement of the antenna gain in an angular range of $\pm$ 55° with a maximum required relative permittivity of 2.9. The work [52] also reported that by increasing the AR layer thickness, one could improve the impedance matching at the expense of decreasing the maximum antenna gain for very broad scan angles. Therefore, it is necessary to pay more attention to the AR layer design to attain broad scan angles over $\pm$ 70°, as shown in [24], [40], [53]. This scenario is further investigated in section C.

The design process of the flattened QCTO Luneburg lens can be divided into 5 steps:

1) Quasi-conformal mapping of the original Luneburg lens permittivity profile in the given virtual space (Eq. 1) onto the permittivity profile in the physical space (Eqs. 2–3).
2) Limiting the resulting permittivity profile to the maximum and minimum values achievable by a ceramic 3D printing process using the alumina ceramics for the selected building unit cell (cross).
3) Creating the discretized 3D model (solid cubes in Fig. 3b) by using customized MATLAB code for the full-wave simulations in CST Studio Suite.

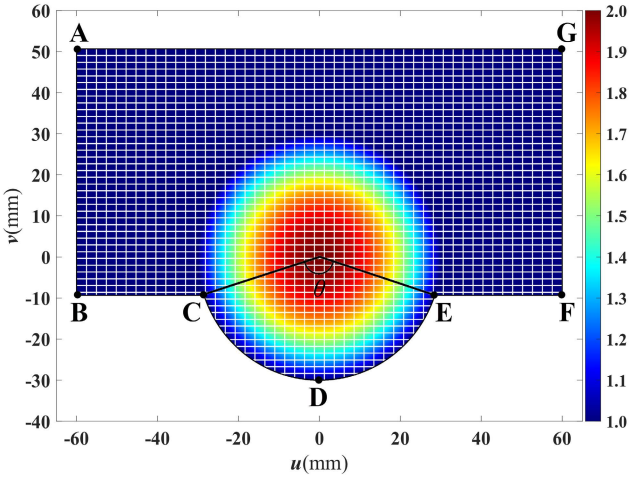

FIGURE 1. The geometry of the virtual space containing the Luneburg lens with a diameter of 60 mm, centered at the origin. The relative permittivity profile of Eq. 1 is presented. The white lines are the vertical *u*-constant and horizontal *v*-constant lines.

4) Assigning the targeted 3D permittivity distribution of the QCTO lens to the closest available permittivity values for the selected unit cell (Fig. 11).
5) Replacing the solid cubes by the crosses with corresponding dimensions for creation of the suitable 3D printing fabrication model (Fig. 13).

A. QUASI-CONFORMAL MAPPING OF THE LUNEBURG LENS

We assume that the Cartesian coordinates that define the virtual and physical spaces are (u, v) and (x, y), respectively. The virtual space is a rectangle with a height of 60 mm and a width of 120 mm that is attached to the Luneburg lens with a diameter of 60 mm. The bottom-left corner of the rectangle is at (−60 mm, −9.33 mm). The relative permittivity of the virtual space follows the below equation (1):

$$\varepsilon_{\mathrm{r}} = \begin{cases} 2 - \dfrac{u^2 + v^2}{R^2} & \text{for } \left|u^2 + v^2\right| \le R^2 \\ 1 & \text{elsewhere,} \end{cases} \tag{1}$$

where R is the radius of the lens (30 mm) that is centered at the coordinate's origin. The virtual space and the vertical u-constant and horizontal v-constant lines are depicted in Fig. 1 as well as the relative permittivity of the virtual space. The $\theta \approx 144°$ angle defines the lens steering angle.

The physical space is a rectangle with side lengths equal to AB and AG. The curved bottom boundary of the Luneburg lens CDE is flattened by the transformation. The quasi-conformal transformation between the virtual and physical spaces is calculated by solving the Laplace's equation in the virtual space for the variables x and y.

The following equations (2) represent the underlying differential equations and the Dirichlet and Neumann boundary

conditions involved in the process.

$$\begin{cases} \nabla^2 x = 0 \\ x|_{\mathrm{AB}} = -60 \\ x|_{\mathrm{FG}} = 60 \\ \partial x/\partial N|_{\mathrm{AG,BC,CD,DE,EF}} = 0, \end{cases} \quad \begin{cases} \nabla^2 y = 0 \\ y|_{\mathrm{AG}} = 60 \\ y|_{\mathrm{BC,CD,DE,EF}} = 0 \\ \partial y/\partial N|_{\mathrm{AB,FG}} = 0, \end{cases} \tag{2}$$

where N is the normal vector of the boundary. The above equations can be solved using MATLAB [55] or COMSOL [56] PDE solvers. After solving the Laplace's equations, the $x(u, v)$ and $y(u, v)$ functions and their partial derivatives are derived. The permittivity distribution in the physical space is calculated by the following equation (3):

$$\varepsilon_{\mathrm{r}}' = \frac{\varepsilon_{\mathrm{r}}}{x_u y_v - x_v y_u}, \tag{3}$$

where the sub-scripts denote partial derivatives.

The permittivity profile of the physical space and the corresponding mapped u-constant and v-constant lines are depicted in Fig. 2a. Note that the corresponding image points are labeled with a prime sign. The images of physical space's x-constant and y-constant lines in the virtual space are depicted in Fig. 2b. The mapped physical space's relative permittivity is included as well.

The original untransformed spherical Luneburg lens has a diameter of 60 mm, while the transformed flattened Luneburg lens has a bottom diameter of 34 mm and the center diameter of 52 mm while the minimum relative permittivity is limited to the value of 1. The height of the lens is then limited by the height of the physical space (60 mm) with the minimum relative permittivity of 1.11. The relative permittivity values below 1 are omitted because we focus on the implementation involving only dielectric materials. In addition, due to minimum achievable effective relative permittivity of the cross unit cell used for the alumina ceramic 3D printing fabrication process, which is about $\varepsilon_{\mathrm{r,eff}} = 1.27$ (see Section V), the transformed QCTO Luneburg lens is further evaluated in a manufacturable region with a bottom diameter of 34 mm, a center diameter of 44 mm and a height of 32 mm. After calculations of the lens relative permittivity distribution in COMSOL Multiphysics, the in-house MATLAB codes were created and exploited for generating a discretized lens for CST Studio Suite (Fig. 3).

The calculated maximum and minimum relative permittivity of the QCTO Luneburg lens is then 8.89 and 1.25, respectively. The relation between the maximum relative permittivity of the transformed lens and the half beam steering angle $\theta/2$, is shown in Fig. 4. Our numerical calculation corresponds to the approach presented by Kundtz *et al.* in [40]. However, the calculation done by Biswas *et al.* in [52], [57] leads to the maximum relative permittivity of 4, that is caused by imposing different Dirichlet and Neumann boundary conditions. To verify the COMSOL calculations, we used a simplified lens model discretized into ringed cylinders with

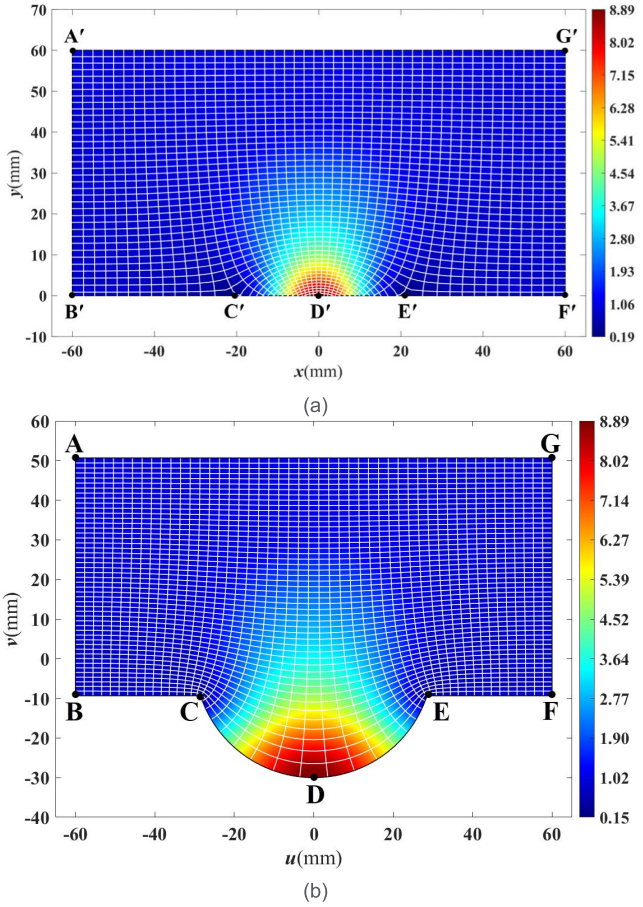

FIGURE 2. (a) Rectangular physical space and its permittivity profile. The white lines are the images of the u-constant and v-constant lines in Fig. 1. (b) The virtual space with the mapped physical space's permittivity profile. The white lines are the images of the x-constant and y-constant lines of the physical space.

the CST time-domain solver in the Ka-band (40 GHz) and the WR-28 waveguide excitation placed at the lens edge. Note that in Fig. 4 we added available results from the literature. Generally, we can see good agreement with our results.

B. QCTO LUNEBURG LENS PERFORMANCE

To evaluate the designed QCTO Luneburg lens, it is assumed that the excitation with the WR-28 waveguide is placed on the lens bottom surface. The numerical simulations in CST Studio Suite were performed in the Ka-band (26.5 GHz to 40 GHz) while the waveguide was shifted from the lens center to the lens edge in 2 mm steps to obtain the radiation patterns in the H-plane (azimuth) (Fig. 5) and the reflection coefficient responses (Fig. 6). The lens antenna realized gain achieves 16.12 dBi at the lens center and 17.31 dBi at the lens edge, steering the beam in the range of $\pm 75°$. The maximum reflection coefficient varies between -3.57 dB and -9.06 dB while shifting the feed position. In the next section, we analyze several impedance transformer profiles to improve the antenna impedance matching.

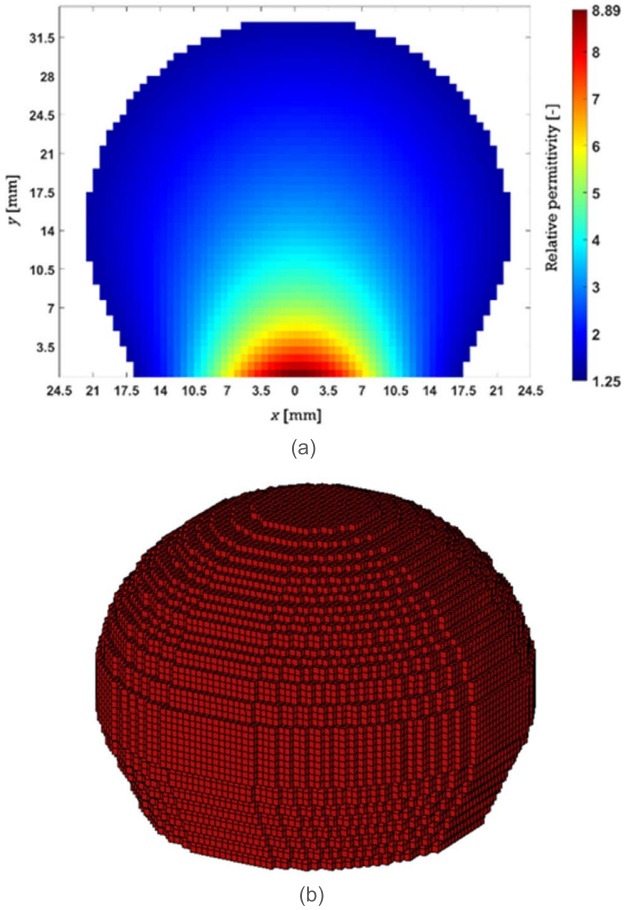

FIGURE 3. (a) Discretized QCTO Luneburg lens in MATLAB, and (b) its geometry in CST Studio Suite. The unit cell size is 0.7 mm × 0.7 mm × 0.7 mm.

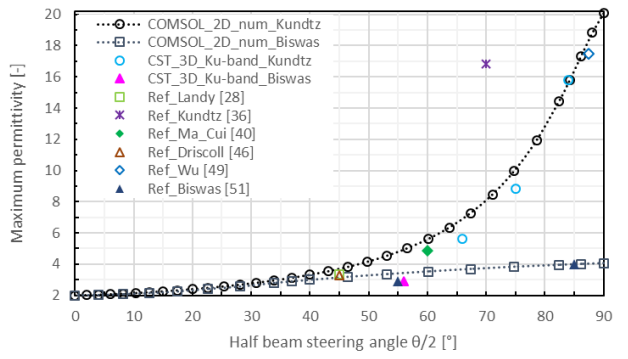

FIGURE 4. Relation between the maximum required relative permittivity of the transformed Luneburg lens and the half beam steering angle. The dotted curves correspond to an internal half-angle $\theta/2$ of original Luneburg lens. Simulated results are compared with references.

C. IMPEDANCE MATCHING LAYER

The effect of adding IML as an antireflective layer on the lens bottom surface was investigated in [52] with the conclusion that the Klopfenstein impedance matching profile with 0.5 λ_0

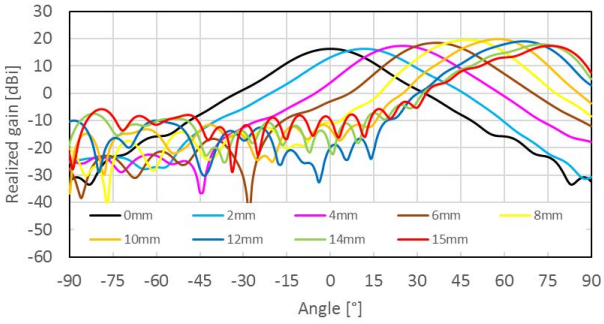

FIGURE 5. Simulated H-plane radiation pattern of the QCTO Luneburg lens excited by a WR-28 waveguide. Position at 0 mm corresponds to the lens center and position at 15 mm corresponds to the lens edge.

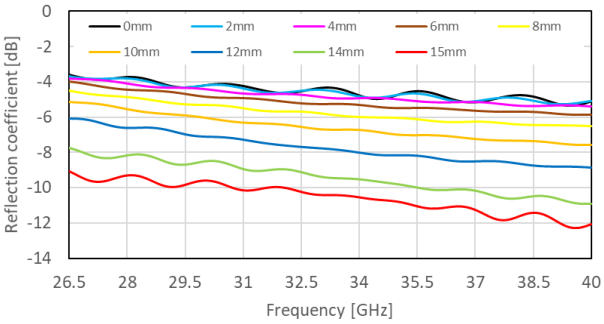

FIGURE 6. Simulated reflection coefficient of the QCTO Luneburg lens excited by a WR-28 waveguide.

layer thickness at the center frequency provides the largest beam steering angle while maintaining a sufficient level of impedance matching. Further, in [57], the exponential and Gaussian impedance matching profiles were evaluated with slightly worse beam steering capabilities. However, these evaluations were carried out on the low maximum relative permittivity ($\varepsilon_r = 2.89$) QCTO Luneburg lens. Since our designed lens has a much higher maximum relative permittivity ($\varepsilon_r = 8.89$), we investigate the combination of the lens and IML on the overall antenna performance for a broadband Klopfenstein, exponential, and Gaussian profiles described by the following equations (4)-(9), respectively [57], [58].

$$\varepsilon_{\mathrm{AR\_Klop}} = \left(\sqrt{\varepsilon_i \varepsilon_l(x,y)} \exp\left[\Gamma_m A^2 \phi\left(2\frac{y}{L} - 1, A\right)\right]\right)^2, \tag{4}$$

$$\Gamma_m = \frac{\Gamma_0}{\cosh A}; \quad \Gamma_0 = \frac{1}{2}\ln\left(\frac{\sqrt{\varepsilon_l}}{\sqrt{\varepsilon_i}}\right), \tag{5}$$

$$\phi(x,A) = \frac{1}{2}\int_0^x \sum_{m=0}^{\infty} \frac{\left(\frac{A^2}{4}\right)^m \left(1-y^2\right)^m}{m!\,(m+1)!} dy, \tag{6}$$

$$\varepsilon_{\mathrm{AR\_exp}} = \left(\sqrt{\varepsilon_i} \exp\left[\frac{y}{L}\ln\left(\frac{\sqrt{\varepsilon_l(x,y)}}{\sqrt{\varepsilon_i}}\right)\right]\right)^2, \tag{7}$$

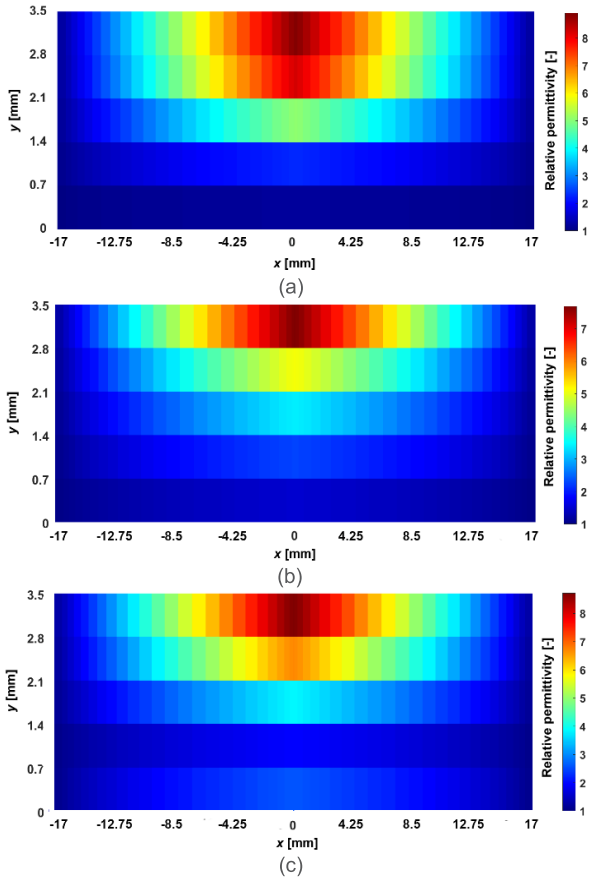

FIGURE 7. 2D discretized impedance matching profiles: (a) Klopfenstein, (b) exponential, (c) Gaussian.

$$\varepsilon_{\mathrm{AR\_Gauss}} = \left(\sqrt{\varepsilon_{\mathrm{i}}}\exp\left[2\left(\frac{y}{\mathrm{L}}\right)^2 \ln\left(\frac{\sqrt{\varepsilon_{\mathrm{l}}(x,y)}}{\sqrt{\varepsilon_{\mathrm{i}}}}\right)\right]\right)^2 \quad \text{for } 0 \le y \le \frac{\mathrm{L}}{2} \tag{8}$$

$$\varepsilon_{\mathrm{AR\_Gauss}} = \left(\sqrt{\varepsilon_{\mathrm{i}}}\exp\left\{\begin{array}{l} 4\left(\frac{y}{\mathrm{L}}\right) - 2\left[\left(\frac{y}{\mathrm{L}}\right)^2 - 1\right]\times \\ \ln\left(\frac{\sqrt{\varepsilon_{\mathrm{l}}(x,y)}}{\sqrt{\varepsilon_{\mathrm{i}}}}\right)\end{array}\right\}\right)^2, \quad \text{for } \frac{\mathrm{L}}{2} \le y \le \mathrm{L} \tag{9}$$

where ε_{i} represents the relative permittivity of free space, ε_{l} is the relative permittivity of the transformed lens gradient-index profile, L represents the antireflective layer thickness, Γ_{m} is the maximum passband ripple (0.001 in our case), the function $\phi\,(x, y)$ describes expanded power series of the first kind Bessel function of the order one, λ_0 is the free-space wavelength at the center frequency.

The discretized impedance matching profiles were implemented by MATLAB codes and are shown in Fig. 7. In our case, the thickness of the broadband IML is chosen to be 0.5 λ_0 (3.5 mm at 40 GHz) to accommodate 5 cells in the longitudinal direction to achieve better manufacturing mechanical stability and the requirement of the integer count of cells (assumed building unit cells size is 0.7 mm × 0.7 mm × 0.7 mm). The influence of the broadband IML on the antenna radiation patterns and the reflection coefficient are depicted in Figs. 8 and 9.

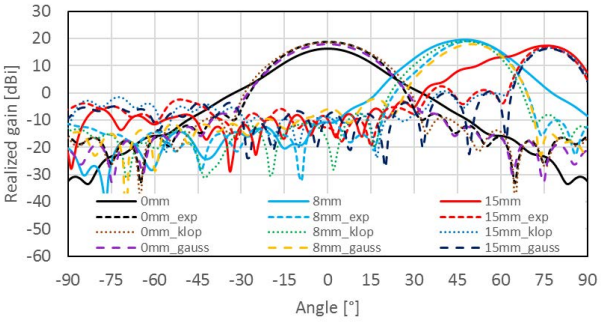

FIGURE 8. Simulated radiation patterns of the QCTO Luneburg lens with an exponential, a Klopfenstein, and a Gaussian IML at a frequency of 40 GHz.

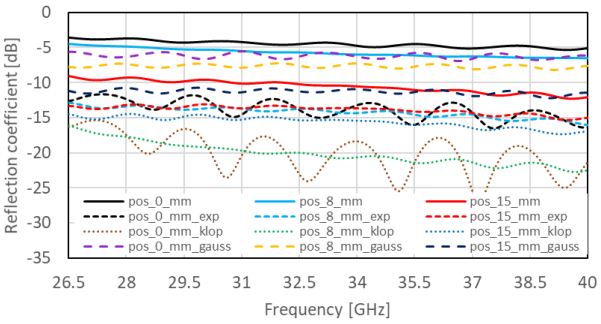

FIGURE 9. Simulated reflection coefficients of the QCTO Luneburg lens with an exponential, a Klopfenstein, and a Gaussian IML.

From the comparison of the broadband IML, the exponential profile provides the largest improvement of the antenna gain while maintaining the maximum beam steering angle of ±75° and the reflection coefficient better than −11.7 dB in the whole Ka-band. Further, the Klopfenstein profile provides a slightly better impedance matching with a reflection coefficient better than −15.4 dB. However, the antenna gain is 0.48 dB less than for the exponential profile at the lens center. In addition, compared to the exponential profile, the Gaussian profile gives 0.95 dB lower antenna gain, and for lens without the IML, the gain improvement of 2.7 dB is achieved at the lens center. The comparison of selected IML and corresponding lens antenna parameters at a frequency of 40 GHz is summarized in Table 2. The higher antenna gain at the lens positions (8 mm; 15 mm) for the case without the IML is caused by a properly located focal point of an excitation waveguide. While for the case of the IML, the focal point is slightly shifted, which could be partially mitigated by creating a multi-sectional IML of different thicknesses as proposed in [57]. Due to those facts, the exponential IML is chosen for manufacturing.

III. FABRICATION AND MEASUREMENTS

A. LENS MODELS INVOLVING FABRICATION LIMITS

The designed flattened QCTO Luneburg lens must be discretized into unit cells which can be fabricated by the ceramic

TABLE 2. QCTO Luneburg lens antenna parameters with different IML at various position of the lens excitation at a frequency of 40 GHz.

Excitation position	Impedance matching layer (Antenna gain [dBi] / Reflection coefficient [dB])			
	Exponential	Klopfenstein	Gaussian	None
0 mm	18.83/-11.7	18.35/-15.4	17.88/-5.6	16.12/-3.6
4 mm	18.76/-11.8	18.51/-15.3	17.85/-6.0	15.01/-3.8
8 mm	19.10/-12.9	18.90/-16.0	17.93/-7.7	19.46/-4.5
12 mm	18.01/-14.0	17.97/-16.3	17.27/-9.6	16.67/-6.1
15 mm	16.68/-13.3	16.52/-14.5	16.27/-11.2	17.31/-9.1

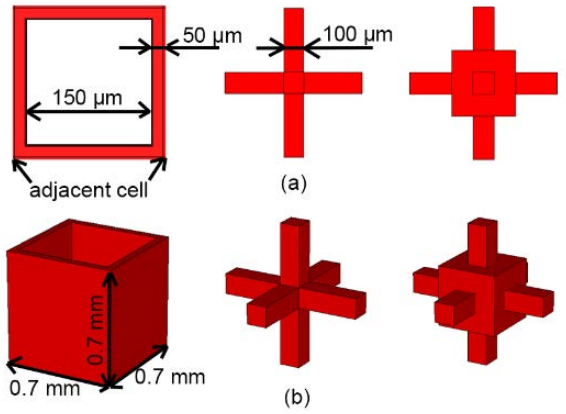

FIGURE 10. Unit cell types used in the ceramic 3D printing and their minimum inner structure's dimensions: squared hole block (not in scale), cross, cube with rods (from left to right), (a) top view, (b) 3D view. The unit cell size is 0.7 mm × 0.7 mm × 0.7 mm.

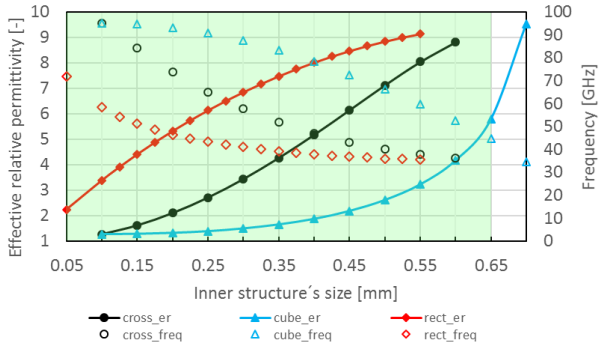

FIGURE 11. Effective relative permittivity of the selected unit cells and the corresponding eigenfrequencies for which the permittivity value is valid. The green area shows the 3D printable region.

3D printing process applied for this study [25], [26]. These unit cell types should be ideally isotropic and easily manufacturable, such as crosses [59] and cubes with rods [60], [61] suitable for 3D objects, or square hole blocks [62] and cylindrical hole blocks [63] applicable for 2D objects.

In our design, we first evaluated the effective relative permittivity of the following unit cell types: crosses, cubes with rods and square hole blocks depicted in Fig. 10 by the numerical simulation of dispersion diagrams [64]. The effective relative permittivity and corresponding eigen-frequencies for

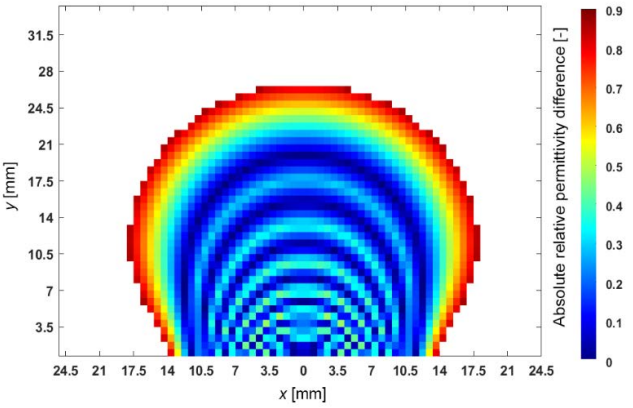

FIGURE 12. Absolute difference between the ideal and achievable effective relative permittivity of the QCTO Luneburg lens (fabricated version) in 3D version composed of the cross unit cells.

which the permittivity value is valid are shown in Fig. 11. A 90° phase shift with E-field oriented in the vertical direction across the unit cell is assumed and the inner structure's dimensions are varied (squared hole size, cross's rod thickness, cube size for 100 μm thick connecting rods). To ensure the success of the ceramic 3D printing process, we need to consider the effect of over polymerization (i.e., unwanted polymerization in vicinity of illuminated pixels, due to the light scattering during printing) and set the minimum inner dimensions to 100 μm (cross, cube with rods), or 50 μm (squared hole block) which results in a 100 μm wall thickness between adjacent cells. Furthermore, the minimum separation between each wall is 150 μm, and the overall unit cell dimensions must be a multiple of 25 μm due to the minimum 3D printer's pixel size. To comply with the trade-off between those limits and the maximum operational frequency of the lens, the overall selected unit cell size is 0.7 mm × 0.7 mm × 0.7 mm.

The alumina relative permittivity used for our design is 9.5 [25], leading to the effective relative permittivity values between 1.27 and 8.81, 1.27 and 5.77, and 2.23 and 9.13 in the cases of cross, cube with rods and square hole unit cells, respectively. According to this comparison, it is clear that the cross unit cell provides the best ability to vary the effective relative permittivity, which follows a nearly linear slope, while for the cube with rods, the effective relative permittivity increases exponentially and is limited to the maximum cube size of 0.65 mm. The squared hole unit cell shows a logarithmic increase of the effective relative permittivity, and its minimum achievable value is limited by the minimum wall thickness. We choose the cross unit cells for the 3D lens fabrication models based on this analysis. The ideal lens permittivity profile will differ from the actual one due to the limited number of feasible effective relative permittivity values for each unit cell type. The absolute difference of the spatial effective relative permittivity distribution between the ideal and the fabricated QCTO Luneburg lens is plotted in Fig. 12.

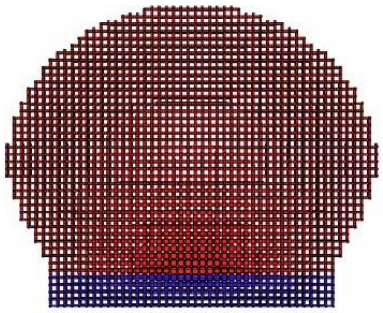

FIGURE 13. Fabrication model of the QCTO Luneburg lens composed of cross unit cells is shown in red color and the exponential IML is shown in blue color. The structure is cut in the middle.

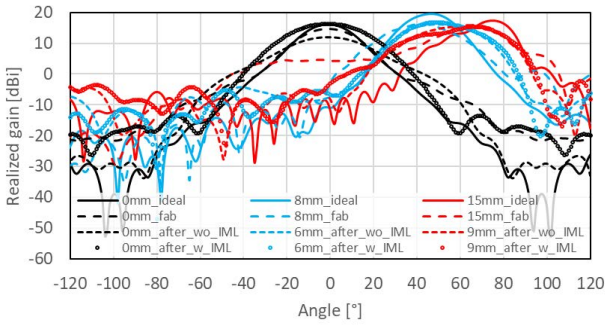

FIGURE 14. Simulated radiation patterns of the QCTO Luneburg lens involving non-ideal spatial permittivity distribution [fab] and the final fabrication dimensions [after] at a frequency of 40 GHz.

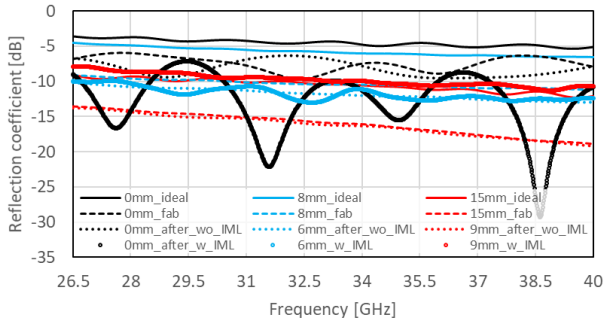

FIGURE 15. Simulated reflection coefficients of the QCTO Luneburg lens involving non-ideal spatial permittivity distribution [fab] and the final fabrication dimensions [after].

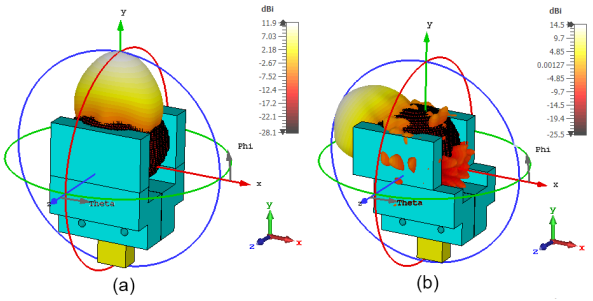

FIGURE 16. 3D radiation patterns of the 3D QCTO Luneburg lens without exponential IML (realized gain) using solid fabrication models, (a) feed at the lens center; (b) feed at the lens edge.

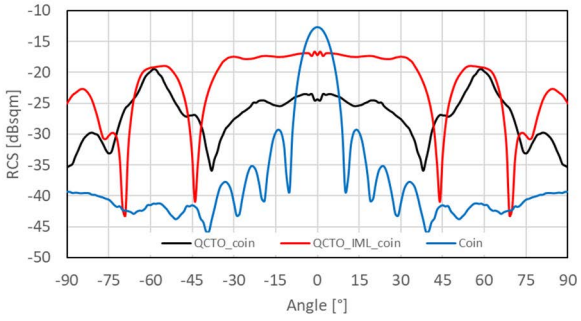

FIGURE 17. Simulated RCS of the QCTO Luneburg lens fabrication version with and without exponential IML.

The mean absolute relative permittivity difference is 0.1465, with the greatest absolute relative permittivity differences concentrated at the lens's outer surface areas. The 3D printer limits the size of the green body to 64 mm × 40 mm × 100 mm. Further, the expected shrinkages caused by sintering are 1.22 and 1.28 in the *xy* plane and *z* direction (i.e., height), respectively. As a result, the maximum dimensions after sintering are restricted to 52 mm × 32 mm × 78 mm. Therefore, the designed lens was recalculated to comply with the green body requirements, reaching a middle diameter of 36.4 mm, a bottom diameter of 28 mm, and a height of 25.9 mm. The example of the fabricated model including the exponential IML is depicted in Fig. 13. The comparison of lens antenna radiation patterns and reflection coefficient involving non-ideal permittivity distribution and lens size after final fabrication (including all size reductions) are shown in Figs. 14 and 15. The focal points of the reduced size lens were shifted accordingly to match the beam steering direction of the original size of the lens.

The non-ideal lens permittivity distribution leads to slightly reduced antenna gain at the lens center position (1.2 dB), but increased gain and decreased beam steering angle at the lens edge positions (up to 2.9 dB and 7 degrees). Due to the lens size reduction, the antenna gain and maximum beam steering capability are further reduced (up to 2.4 dB and 3 degrees), so the maximum beam steering angle of the designed lens is ±65°. By adding the IML, the antenna gain is further increased by 4.4 dB to the value of 16.23 dBi for the boresight direction. The 3D radiation patterns of the 3D QCTO Luneburg lens, including the full measurement setup (the lens with a holder and a metallic waveguide probe) are shown in Fig. 16. It can be observed that the designed lens holder has a minor effect on the lenses' radiation patterns since it is designed as an open structure in the lenses' radiation directions.

To evaluate the fabrication version of the QCTO Luneburg lens as a retroreflector, a circular metallic part with a diameter of 25.75 mm and thickness of 2.20 mm is placed on the

lens's bottom, simulating a 2 EUR coin employed as the reflective metallic layer. The simulated angular RCS response at a frequency of 40 GHz for the metallic coin and the lens with and without the exponential IML is depicted in Fig. 17. From the comparison, it is obvious that the IML improves the overall RCS and achieves a more stable response over a large angular range. It is shown that the QCTO retroreflective lens presents a maximum RCS of −24.3 dBsqm, while the QCTO retroreflective lens with the IML has a maximum RCS of −17.16 dBsqm at boresight. The abrupt RCS drop near angle of ±45° is caused by a destructive interference of the incoming and reflected EM wave.

B. QCTO LUNEBURG LENS FABRICATION

The lithography-based ceramic manufacturing (LCM) technology was employed for the realization of the discussed lens structures. With this 3D printing method, lens's parts are created layer-by-layer via DLP-controlled polymerization of a photosensitive slurry [65], [66]. The utilized printer was a Lithoz CeraFab 7500 [67] with a printing resolution of 25 μm and a UV light source (wavelength: ∼450 nm) for slurry polymerization.

Lens's parts were printed using a newly formulated slurry (i. e., LithaLox 360 [67]) and with an illumination energy of 450 mJ/cm^2/layer. LithaLox 360 was intentionally developed for the fabrication of delicate samples, such as the Luneburg lens structures and contains 49 vol% of high purity Al2O3 powder as well as 51 vol% of UV-curable polymers. Directly after printing, the parts were cleaned to wash out the residual unpolymerized slurry. This was done by dipping the samples in LithaSol 20 [67] cleaning fluid, letting them soak for 5 minutes, and then ultrasonication of the system for 2 minutes. To ensure the cleanness of the samples, especially inside the lens's narrow holes and channels, the cleaning process was repeated 10 times for each sample.

Afterward, the following thermal processing steps were performed to convert the cleaned green samples to dense ceramics parts. First, samples were slowly dried in an electrical laboratory dryer. The maximum temperature and duration of the drying step were 140°C and 6 days, respectively. The dried samples were then sintered in another electric furnace and under ambient atmosphere. Since the dried parts still consisted of 51 vol% of cured polymers, heating rates were low up to temperatures of 430°C (i.e., the temperature by which polymer compounds will be fully decomposed into volatile components) to guarantee the fabrication of crack-free samples. In this study, the lens's parts were sintered at 1600°C, and the sintering duration was 4 days. The fabricated lenses are illustrated in Fig. 18 where the lenses are illuminated with a light source to appreciate their solid core through the whole grid array structure.

C. LENS ANTENNA CHARACTERIZATION

The measurement of the radiation pattern was performed in an anechoic chamber with the antenna scanner NSI 700S-30 and a Vector Network Analyzer (VNA) R&S ZVA67

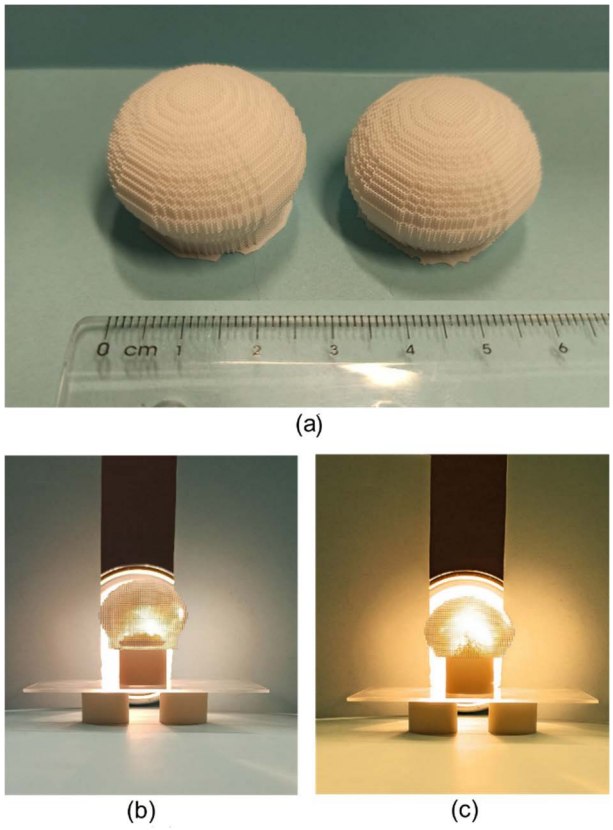

FIGURE 18. (a) Fabricated samples of the 3D QCTO Luneburg lens (right) and the lens with exponential IML (left), (b) and (c) manufactured lens with and without IML, respectively, illuminated by a torch to appreciate their solid core.

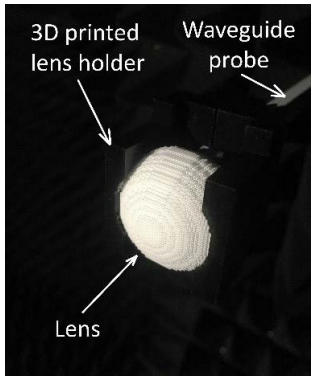

FIGURE 19. Measurement setup of QCTO Luneburg lens antenna with a lens holder in the anechoic chamber.

with a 23 dBi horn antenna used as a transmitting antenna. A standard WR-28 waveguide probe was used with the lens as a receiving antenna. The lens was sequentially placed into individual 3D printed holders with a gradually shifted excitation position by 3 mm to precisely control the excitation position. The arm with lens was then rotated in 1-degree steps by a computer controller. The lens with holder in the anechoic chamber is shown in Fig. 19. The measured gain of the QCTO Luneburg lens is shown in Fig. 20.

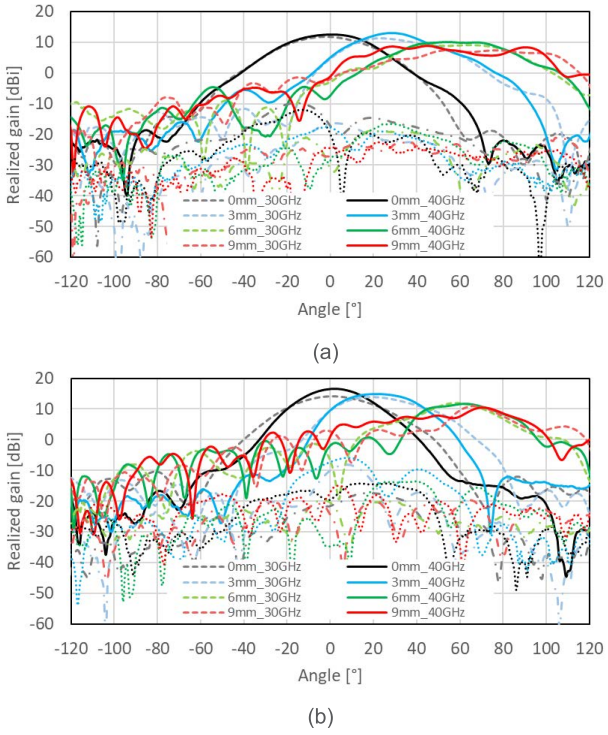

FIGURE 20. Measured radiation patterns of the fabricated 3D QCTO Luneburg lens: (a) without the IML, (b) with the IML. The cross-polarization component is shown as dotted (30 GHz) and dash-dotted (40 GHz) lines.

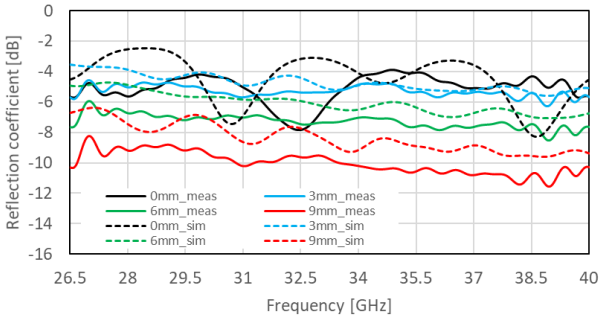

FIGURE 21. Measured and simulated reflection coefficient of the fabricated 3D QCTO Luneburg lens without the IML.

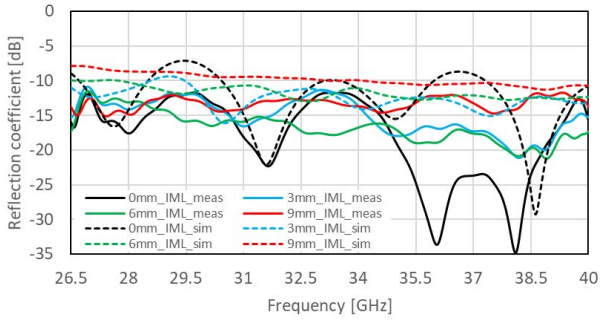

FIGURE 22. Measured and simulated reflection coefficient of the fabricated 3D QCTO Luneburg lens with the IML.

For the lens without the IML, the gain is 12.62 dBi at 40 GHz at the lens center. Due to the radiation pattern flatness, the measured gain at the lens edge achieves 8.75 dBi and 8.25 dBi with the maximum beam steering angle of 45° and 90°, respectively. The measured gain of the lens with the exponential IML at 40 GHz is 16.51 dBi at the lens center and 10.49 dBi at the lens edge with the maximum beam steering angle of 70°. It is obvious that IML improves the gain of the lens by nearly 4 dB. The input reflection coefficient responses of the lens for different positions with and without the IML is shown in Figs. 21 and 22. The improvement caused by the IML is significant mainly for the lens center position. The input reflection coefficient is lower than −10 dB in the whole Ka-band. Those values are in good agreement with the simulation results. The discrepancy of the measured gain for higher beam steering directions can be caused by the excessive alumina material trapped inside the lens which could not be removed during fabrication, and the interaction of the wave with the lens holder.

D. RETROREFLECTIVE LENS CHARACTERIZATION

The characterization of the lens with reflective layer was performed by employing the Vector Network Analyzer PNA-X N5247A from Agilent Technologies, with its bandwidth set between 30 GHz to 40 GHz and 10001 frequency points, as well as IF bandwidth of 5 kHz. The measurements were performed with an 18 dBi Ka-band horn antenna, connected to a right angle (90°) WR-28 waveguide to coaxial adapter, and then to the VNA via a K-V transition and a V(m)-V(f) cable. Moreover, the structures are located within the transmitting/receiving horn antenna's far field, at a distance of 0.3 m. The corresponding measurement setup is displayed in Fig. 23. In this case, the reflective layer was implemented by a metallic 2 EUR coin, whereas an electronically controlled turntable was used to perform angular measurements with 1° resolution. For each angle, a reference measurement without the tag was taken and subtracted from the raw data, to remove the influence of reflections from the horn antenna, as well as reflections from the surrounding environment. The measured reflection coefficients for the employed coin, as well as the two fabricated lenses with and without the coin as the reflective layer, are presented in Fig. 24.

The results in Fig. 24 show that the backscattered power is higher when the coin is added at the bottom of each lens. Concretely, in the case of lens with matching layer, the backscattered power is an average 7.5 dB larger than when no metal coin is employed as reflective layer. In the case of the lens without IML, the backscattered power when the coin is added is less than its coin-less counterpart between 31.5 GHz and 36.5 GHz. This is attributed to an interaction between the high-ε_r lens's core and the metallic coin, but more research needs to be conducted to ascertain the concrete

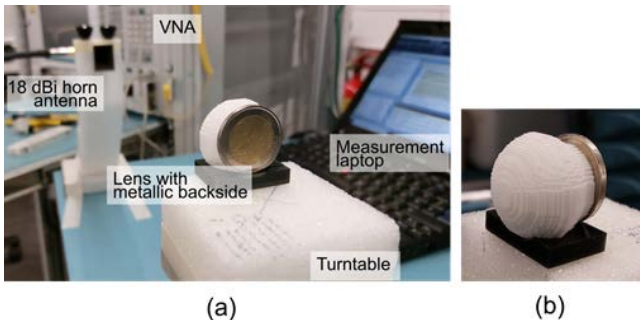

FIGURE 23. (a) Measurement setup for the retroreflective lens characterization, and (b) front view of the combination of lens and coin.

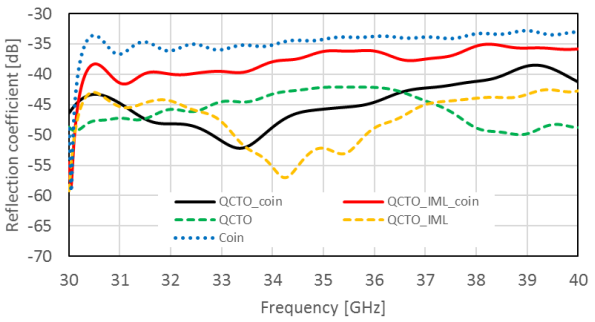

FIGURE 24. Measured reflection coefficient for the frontal incidence in the frequency-domain.

reason. Regardless, when the coin is added, the lens without the IML increases its backscattered power by an average of 1.3 dB.

The monostatic radar cross-section (RCS) is a normalized measurement of the backscattered power of a structure, independent of the distance between the structure and the monostatic radar antenna. When employing a radar target with known RCS, the unknown RCS of a reflective structure is calculated by (10):

$$RCS_{\text{tag}} = RCS_{\text{ref}} \cdot \frac{|S_{11,\text{tag}}|^2}{|S_{11,\text{ref}}|^2}, \tag{10}$$

where $|S_{11}|$ is the measured reflection coefficient, *tag* corresponds to the retroreflective lens-based structure and *ref* is the radar target employed as reference for calculating the RCS.

A corner reflector (CR) with an edge of 8.3 cm is employed as a reference radar target, with an analytical RCS in boresight at 40 GHz of 5.48 dBsqm, according to (11) [69]:

$$RCS_{\text{CR(ref)}} = 10 \log \left(\frac{4\pi}{3} \cdot \frac{a^4}{\lambda_0^2} \right), \tag{11}$$

where a denotes the corner reflector's edge and λ_0 is the free-space wavelength.

When the CR is placed at a distance of 0.3 m from the horn antenna, the latter is not located in the far field of the former, which starts at 3.67 m. Therefore, the RCS cannot

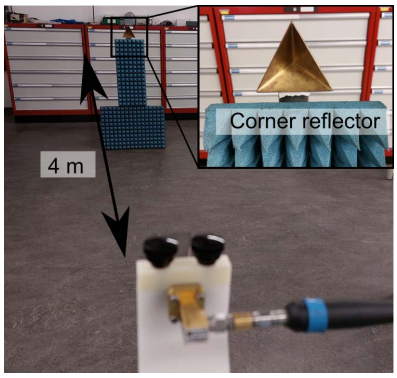

FIGURE 25. Measurement setup for the corner reflector with an 8.3 cm edge employed as a known radar target for RCS computation. The analytical RCS in boresight at 40 GHz is $RCS_{\text{ref}} = 5.48$ dBsqm.

be computed accurately with (10) and (11). Instead, the CR is measured when placed 4 m away from the horn antenna. Then, the magnitude of the received S_{11} in frequency-domain is predicted at a distance of 0.3 m by considering the received power P_r in a monostatic radar system (12):

$$P_r = \frac{P_t G_t^2 \lambda_0^2 RCS_{\text{target}}}{(4\pi)^3} \cdot \frac{1}{d^4}, \tag{12}$$

where P_t is the transmitted power, G_t is the horn antenna gain, and d the distance between radar and target. Assuming the same measurement setup is employed for different distances, P_t, G_t and $\text{RCS}_{\text{target}}$ remain constant. Thus, by dividing Eq. (12) for the two different distances of 0.3 m and 4 m, the following relation between the corresponding $|S_{11}|$ is obtained:

$$|S_{11,\,0.3\text{ m}}|^2 = |S_{11,4\text{ m}}|^2 \cdot \left(\frac{4\text{ m}}{0.3\text{ m}} \right)^4, \tag{13}$$

It should be pointed out that (13) is only accurate when (i) the measurement of the corner reflector is in line-of-sight, (ii) the distance at which the $|S_{11}|$ is predicted is within the far field of the transmitting horn antenna, and (iii) the same monostatic radar setup is employed for both retroreflective lens and corner reflector measurements, which is our case.

The corresponding measurement setup for the corner reflector is shown in Fig. 25, whereas the received backscattered signals of the corner reflector are presented in Fig. 26. Empty room subtraction and time gating between 26 ns to 28 ns are employed to minimize the influence of the surrounding environment.

The calculated RCSs at 40 GHz for the QCTO-based retroreflective lens with and without IML are presented in Fig. 27. It is shown that the QCTO retroreflective lens presents a maximum RCS of −20.05 dBsqm at the angle of −7°, whereas the QCTO retroreflective lens with IML has a maximum RCS of −15.78 dBsqm for the frontal incidence. Both values are 6.85 dB and 2.67 dB below the single coin's RCS for the frontal incidence, respectively.

Furthermore, the retroreflective lenses also present a wide angular range where the backscattered power remains with

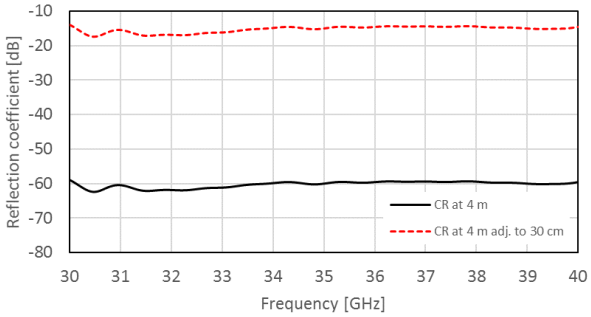

FIGURE 26. Measured and adjusted reflection coefficient for the corner reflector.

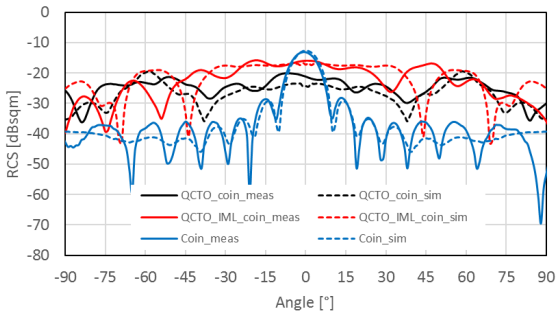

FIGURE 27. Measured and simulated RCS over angle at a frequency of 40 GHz.

relatively high magnitude. The operating angular range, defined between the angles in which the RCS decreases by 10 dB regarding the maximum value, is ±7° for the coin, ±37° for the lens and ±50° for the lens with IML. The retroreflective structures present less angular range than the maximum steerable angle of the designed lens. This is owing to the finite size of the metallic coin used as reflective layer. As the lens is rotated, the effective size of the coin is smaller, which in turn reflects less power.

The radar range equation (12) is used to calculate the maximum read-out range with our setup by solving it for the distance. In our measurements, P_t is −5 dBm, G_t is 18 dBi, λ_0 is set to the vacuum wavelength at 40 GHz and P_r is set to the minimum detectable power at the receiver, $P_{r,min}$, which is −70 dBm. With these values, the maximum read-out ranges are 48.63 cm and 62.18 cm for the retroreflective lens without and with IML, respectively.

IV. CONCLUSION

In this paper, we have proposed a novel 3D QCTO based Luneburg lens for Ka-band mm-wave self-localization systems, which has been manufactured from high permittivity alumina with the LCM 3D printing process. The maximum realized gain of the lens without an IML is 12.62 dBi, and the lens with the exponential IML led to the maximum realized gain of 16.51 dBi at 40 GHz with the maximum beam steering angles of 90° and 70°, respectively. The comparison with other related works is summarized in Table 3. The maximum RCS of the lens backed by a reflective layer, which is firstly evaluated for this kind of retroreflector, without and with the exponential IML is −20.05 dBsqm and −15.78 dBsqm at 40 GHz, respectively.

TABLE 3. 3D printed ceramic Luneburg lens antennas.

Ref.	Frequency [GHz]	Max. beam steering angle [°] / lens type	Max. gain @ Freq. [dBi]	Dimensions [mm] (w x h)
[59]	28–38	fixed at 0 / 3D	26 (33)	54 x 54
[62]	12–18	±20 / 2D	19.1 (18)	70.9 x 7.9
[63]	12–18	±15 / 2D	16.5 (13)	70.04 x 7.94
[68]	12–18	fixed at 0 / 2D	18 (n/a)	70 x 8
This work	**26.5–40**	**±70 / 3D**	**16.51 (40)**	**29.9 x 23.2**

To the best of the authors' knowledge, this is the first demonstration of a 3D and retroreflective ceramic QCTO Luneburg lens. The employment of ceramics such as alumina for the lens allows for the realization of wide-angle frequency-coded retroreflectors that can be used for mm-wave indoor localization in dynamic cluttered harsh and high-temperature environments, e.g., withstanding a fire. Future development will be focused on the integration of the lens with 3D photonic crystal-based frequency-coding particles into a monolithic block, and their placement along the lens's bottom, with the objective of achieving angle-of-arrival identification.

ACKNOWLEDGMENT

(Petr Kaděra and Jesús Sánchez-Pastor contributed equally to this work.)

REFERENCES

[1] D. Desai, I. Gatley, C. Bolton, L. Rizzo, S. Gatley, and J. F. Federici, "Terahertz Van Atta retroreflecting arrays," *J. Infr., Millim., THz Waves*, vol. 41, no. 8, pp. 997–1008, Jun. 2020.

[2] A. B. Numan, J.-F. Frigon, and J.-J. Laurin, "Wide field of view retrodirective millimeter wave antenna array with pulse modulation and orthogonal polarization states," *IEEE Access*, vol. 8, pp. 221127–221137, 2020.

[3] A. Jiménez-Sáez, A. Alhaj-Abbas, M. Schüßler, A. Abuelhaija, M. El-Absi, M. Sakaki, L. Samfaß, N. Benson, M. Hoffmann, R. Jakoby, T. Kaiser, and K. Solbach, "Frequency-coded mm-wave tags for self-localization system using dielectric resonators," *J. Infr., Millim., THz Waves*, vol. 41, no. 8, pp. 908–925, Jun. 2020.

[4] J. Sanchez-Pastor, A. Jimenez-Saez, M. Schusler, and R. Jakoby, "Gridded square-ring frequency selective surface for angular-stable response on chipless indoor location tag landmarks," in *Proc. 15th Eur. Conf. Antennas Propag. (EuCAP)*, Düsseldorf, Germany, Mar. 2021, pp. 1–5.

[5] J. Barowski, A. Alhaj-Abbas, M. El-Absi, L. Piotrowsky, N. Pohl, I. Rolfes, and K. Solbach, "Design and evaluation of a passive frequency-coded reflector using W-band FMCW radar," in *Proc. German Microw. Conf. (GeMiC)*, Cottbus, Germany, Mar. 2020, pp. 92–95.

[6] M. El-Absi, A. A. Abbas, A. Abuelhaija, F. Zheng, K. Solbach, and T. Kaiser, "High-accuracy indoor localization based on chipless RFID systems at THz band," *IEEE Access*, vol. 6, pp. 54355–54368, 2018.

[7] K. Solbach, A. A. Abbas, M. El-Absi, A. Abuelhaija, and T. Kaiser, "Experimental demonstration of double-notch RCS spectral signature of corner reflector tag for THz self-localization system," in *Proc. 3rd Int. Workshop Mobile THz Syst. (IWMTS)*, Essen, Germany, Jul. 2020, pp. 1–4.

[8] R. J. Williams, A. J. Gatesman, T. M. Goyette, and R. H. Giles, "Radar cross section measurements of frequency selective terahertz retroreflectors," *Proc. SPIE*, vol. 9102, May 2014, Art. no. 91020R.

[9] J. Sanchez-Pastor, A. Jimenez-Saez, M. Schuessler, and R. Jakoby, "Frequency-coded spherical retroreflector for wide-angle indoor localization tag landmarks," in *Proc. 4th Int. Workshop Mobile THz Syst. (IWMTS)*, Essen, Germany, Jul. 2021, pp. 1–5.

[10] A. Jimenez-Saez, M. Schusler, D. Pandel, N. Benson, and R. Jakoby, "3D printed 90 GHz frequency-coded chipless wireless RFID tag," in *IEEE MTT-S Int. Microw. Symp. Dig.*, Bochum, Germany, Jul. 2019, pp. 4–6.

[11] A. A. Abbas, Y. Zantah, K. Solbach, and T. Kaiser, "Frequency-coded lens by photonic crystal resonator for mm-wave chipless RFID applications," in *Proc. 4th Int. Workshop Mobile THz Syst. (IWMTS)*, Essen, Germany, Jul. 2021, pp. 1–5.

[12] P. Kadera, A. Jimenez-Saez, L. Schmitt, M. Schusler, M. Hoffmann, J. Lacik, and R. Jakoby, "Frequency coded retroreflective landmark for 230 GHz indoor self-localization systems," in *Proc. 15th Eur. Conf. Antennas Propag. (EuCAP)*, Düsseldorf, Germany, Mar. 2021, pp. 1–5.

[13] P. Kadera, A. Jimenez-Saez, T. Burmeister, J. Lacik, M. Schusßler, and R. Jakoby, "Gradient-index-based frequency-coded retroreflective lenses for mm-wave indoor localization," *IEEE Access*, vol. 8, pp. 212765–212775, 2020.

[14] R. A. Bahr, A. O. Adeyeye, S. Van Rijs, and M. M. Tentzeris, "3D-printed omnidirectional Luneburg lens retroreflectors for low-cost mm-wave positioning," in *Proc. IEEE Int. Conf. RFID (RFID)*, Orlando, FL, USA, Sep. 2020, pp. 1–7.

[15] Y.-Q. Liu, S. Li, J. Guo, L. Li, and H. Yin, "Planar microwave retroreflector based on transmissive gradient index metasurface," *New J. Phys.*, vol. 22, no. 6, Jun. 2020, Art. no. 063044.

[16] A. Arbabi, E. Arbabi, Y. Horie, S. M. Kamali, and A. Faraon, "Planar metasurface retroreflector," *Nature Photon.*, vol. 11, pp. 415–421, Jun. 2017.

[17] C. Guan, H. Li, X. Ding, Z. Wang, K. Zhang, M. Jin, S. N. Burokur, J. Liu, and Q. Wu, "Dual-polarized dual-channel helicity-switching or helicity-preserving retroreflectors utilizing 1-bit coding metasurfaces," *ACS Appl. Electron. Mater.*, vol. 2, no. 10, pp. 3380–3389, Sep. 2020.

[18] L. Yan, W. Zhu, M. F. Karim, H. Cai, A. Y. Gu, Z. Shen, P. H. J. Chong, D.-L. Kwong, C.-W. Qiu, and A. Q. Liu, "0.2 λ_0 thick adaptive retroreflector made of spin-locked metasurface," *Adv. Mater.*, vol. 30, no. 39, Aug. 2018, Art. no. 1802721.

[19] F. Sun, Y. Liu, Y. Yang, Z. Chen, and S. He, "Arbitrarily shaped retroreflector by optics surface transformation," *Chin. Opt. Lett.*, vol. 18, no. 10, 2020, Art. no. 102201.

[20] Y. G. Ma, C. K. Ong, T. Tyc, and U. Leonhardt, "An omnidirectional retroreflector based on the transmutation of dielectric singularities," *Nature Mater.*, vol. 8, no. 8, pp. 639–642, Jun. 2009.

[21] Y. Luo, L.-X. He, S.-Z. Zhu, H. L. W. Chan, and Y. Wang, "Flattening of conic reflectors via a transformation method," *Phys. Rev. A, Gen. Phys.*, vol. 84, no. 2, Aug. 2011, Art. no. 023843.

[22] S. Xiong, Y. Feng, T. Jiang, and J. Zhao, "Designing retrodirective reflector on a planar surface by transformation optics," *AIP Adv.*, vol. 3, no. 1, Jan. 2013, Art. no. 012113.

[23] L. Liang and S. V. Hum, "Wide-angle scannable reflector design using conformal transformation optics," *Opt. Exp.*, vol. 21, no. 2, pp. 2133–2146, Jan. 2013.

[24] P. Kadera, J. Sanchez-Pastor, A. Jimenez-Saez, M. Schusler, J. Lacik, and R. Jakoby, "QCTO Luneburg lens-based retroreflective tag landmarks for mm-wave self-localization systems," in *Proc. IEEE-APS Top. Conf. Antennas Propag. Wireless Commun. (APWC)*, Honolulu, HI, USA, Aug. 2021, pp. 1–4.

[25] A. Jiménez-Sáez, M. Schüßler, C. Krause, D. Pandel, G. von Bögel, N. Benson, and R. Jakoby, "3D printed alumina for low-loss millimeter wave components," *IEEE Access*, vol. 7, pp. 40719–40724, 2019.

[26] J. Ornik, M. Sakaki, M. Koch, J. C. Balzer, and N. Benson, "3D printed Al_2O_3 for terahertz technology," *IEEE Access*, vol. 9, pp. 5986–5993, 2021.

[27] J. B. Pendry, D. Schurig, and D. R. Smith, "Controlling electromagnetic fields," *Science*, vol. 312, no. 5781, pp. 1780–1782, May 2006.

[28] U. Leonhardt, "Optical conformal mapping," *Science*, vol. 312, no. 5781, pp. 1777–1780, 2006.

[29] D. G. Silva, P. A. Teixeira, L. H. Gabrielli, M. A. F. C. Junqueira, and D. H. Spadoti, "Full three-dimensional isotropic carpet cloak designed by quasi-conformal transformation optics," *Opt. Exp.*, vol. 25, no. 19, pp. 23517–23522, 2017.

[30] N. I. Landy, N. Kundtz, and D. R. Smith, "Designing three-dimensional transformation optical media using quasiconformal coordinate transformations," *Phys. Rev. Lett.*, vol. 105, no. 19, Nov. 2010, Art. no. 193902.

[31] H.-X. Xu, G. Hu, Y. Wang, C. Wang, M. Wang, S. Wang, Y. Huang, P. Genevet, W. Huang, and C.-W. Qiu, "Polarization-insensitive 3D conformal-skin metasurface cloak," *Light, Sci. Appl.*, vol. 10, no. 1, p. 75, Apr. 2021.

[32] J. Lei, J. Yang, X. Chen, Z. Zhang, G. Fu, and Y. Hao, "Experimental demonstration of conformal phased array antenna via transformation optics," *Sci. Rep.*, vol. 8, no. 1, p. 3807, Feb. 2018.

[33] F. Sun and S. He, "Extending the scanning angle of a phased array antenna by using a null-space medium," *Sci. Rep.*, vol. 4, no. 1, p. 6832, Oct. 2014.

[34] H. Eskandari, J. L. Albadalejo-Lijarcio, O. Zetterstrom, T. Tyc, and O. Quevedo-Teruel, "H-plane horn antenna with enhanced directivity using conformal transformation optics," *Sci. Rep.*, vol. 11, no. 1, p. 14322, Jul. 2021.

[35] H. Eskandari, S. Saviz, and T. Tyc, "Directivity enhancement of a cylindrical wire antenna by a graded index dielectric shell designed using strictly conformal transformation optics," *Sci. Rep.*, vol. 11, p. 13035, Jul. 2021.

[36] F. Sun and S. He, "Waveguide bends by optical surface transformations and optic-null media," *J. Opt. Soc. Amer. B, Opt. Phys.*, vol. 35, no. 4, pp. 944–949, Apr. 2018.

[37] H. Eskandari, A. R. Attari, M. S. Majedi, and T. Tyc, "Waveguide tapering using conformal transformation optics for ideal transmission," in *Proc. 13th Int. Congr. Artif. Mater. Novel Wave Phenomena, Metamaterials*, Rome, Italy, Sep. 2019, pp. 116–118.

[38] H. Eskandari and T. Tyc, "Controlling refractive index of transformation-optics devices via optical path rescaling," *Sci. Rep.*, vol. 9, no. 1, p. 18412, Dec. 2019.

[39] D. A. Roberts, N. Kundtz, and D. R. Smith, "Optical lens compression via transformation optics," *Opt. Exp.*, vol. 17, no. 19, pp. 16535–16542, Sep. 2009.

[40] N. Kundtz and D. R. Smith, "Extreme-angle broadband metamaterial lens," *Nature Mater.*, vol. 9, no. 2, pp. 129–132, Dec. 2009.

[41] O. Quevedo-Teruel, W. Tang, R. C. Mitchell-Thomas, A. Dyke, H. Dyke, L. Zhang, S. Haq, and Y. Hao, "Transformation optics for antennas: Why limit the bandwidth with metamaterials?" *Sci. Rep.*, vol. 3, no. 1, p. 1903, May 2013.

[42] J. M. Poyanco, F. Pizarro, and E. Rajo-Iglesias, "Wideband hyperbolic flat lens in the Ka-band based on 3D-printing and transformation optics," *Appl. Phys. Lett.*, vol. 118, no. 12, Mar. 2021, Art. no. 123503.

[43] D.-H. Kwon, "Quasi-conformal transformation optics lenses for conformal arrays," *IEEE Antennas Wireless Propag. Lett.*, vol. 11, pp. 1125–1128, 2012.

[44] H. F. Ma and T. J. Cui, "Three-dimensional broadband and broad-angle transformation-optics lens," *Nature Commun.*, vol. 1, no. 1, p. 124, Nov. 2010.

[45] H. Eskandari, M. S. Majedi, A. R. Attari, and O. Quevedo-Teruel, "Elliptical generalized Maxwell fish-eye lens using conformal mapping," *New J. Phys.*, vol. 21, no. 6, Jun. 2019, Art. no. 063010.

[46] C. Mateo-Segura, M. Lorente-Crespo, and Y. Hao, "All dielectric conformal Luneburg lens based antenna," in *Proc. 8th Eur. Conf. Antennas Propag. (EuCAP)*, The Hague, The Netherlands, Apr. 2014, pp. 3001–3004.

[47] Q. Liao, N. J. G. Fonseca, and O. Quevedo-Teruel, "Compact multibeam fully metallic geodesic Luneburg lens antenna based on non-Euclidean transformation optics," *IEEE Trans. Antennas Propag.*, vol. 66, no. 12, pp. 7383–7388, Dec. 2018.

[48] M. Ebrahimpouri and O. Quevedo-Teruel, "Bespoke lenses based on quasi-conformal transformation optics technique," *IEEE Trans. Antennas Propag.*, vol. 65, no. 5, pp. 2256–2264, May 2017.

[49] O. Quevedo-Teruel and Y. Hao, "Directive radiation from a diffuse Luneburg lens," *Opt. Lett.*, vol. 38, no. 4, pp. 392–394, Feb. 2013.

[50] T. Driscoll, G. Lipworth, J. Hunt, N. Kundtz, D. N. Basov, and D. R. Smith, "Performance of a three dimensional transformation-optical-flattened Lüneburg lens," *Opt. Exp.*, vol. 20, no. 12, pp. 13262–13273, Jun. 2012.

[51] O. Quevedo-Teruel, W. Tang, and Y. Hao, "Isotropic and nondispersive planar fed Luneburg lens from Hamiltonian transformation optics," *Opt. Lett.*, vol. 37, no. 23, pp. 4850–4852, Dec. 2012.

[52] S. Biswas and M. Mirotznik, "High gain, wide-angle QCTO-enabled modified Luneburg lens antenna with broadband anti-reflective layer," *Sci. Rep.*, vol. 10, no. 1, p. 12646, Jul. 2020.

[53] L. Wu, X. Tian, M. Yin, D. Li, and Y. Tang, "Three-dimensional liquid flattened Luneburg lens with ultra-wide viewing angle and frequency band," *Appl. Phys. Lett.*, vol. 103, no. 8, Aug. 2013, Art. no. 084102.
[54] R. K. Luneburg and M. Herzberger, *Mathematical Theory of Optics*. Berkeley, CA, USA: Univ. California Press, 1964, pp. 182–188.
[55] MATLAB. *MathWorks* Accessed: Jan. 30, 2022. [Online]. Available: https://www.mathworks.com/products/MATLAB.html
[56] COMSOL. *Multiphysics*. Accessed: Jan. 30, 2022. [Online]. Available: https://www.comsol.com/
[57] S. Biswas, "Design and additive manufacturing of broadband beamforming lensed antennas and load bearing conformal antennas," Ph.D. dissertation, Dept. Elect. Comput. Eng., Univ. Delaware, Newark, DE, USA, 2019.
[58] E. B. Grann, M. G. Moharam, and D. A. Pommet, "Optimal design for antireflective tapered two-dimensional subwavelength grating structures," *J. Opt. Soc. Amer. A, Opt. Image Sci.*, vol. 12, no. 2, p. 333, Feb. 1995.
[59] K. F. Brakora, J. Halloran, and K. Sarabandi, "Design of 3-D monolithic MMW antennas using ceramic stereolithography," *IEEE Trans. Antennas Propag.*, vol. 55, no. 3, pp. 790–797, Mar. 2007.
[60] E. Burden, Y. Oh, B. Mummareddy, D. Negro, P. Cortes, A. D. Plessis, E. MacDonald, J. Adams, F. Li, and R. Rojas, "Unit cell estimation of volumetrically-varying permittivity in additively-manufactured ceramic lattices with X-ray computed tomography," *Mater. Des.*, vol. 210, Nov. 2021, Art. no. 110032.
[61] Y. Oh, V. T. Bharambe, J. J. Adams, D. Negro, and E. MacDonald, "Design of a 3D printed gradient index lens using high permittivity ceramic," in *Proc. IEEE Int. Symp. Antennas Propag. North Amer. Radio Sci. Meeting*, Montreal, QC, Canada, Jul. 2020, pp. 1431–1432.
[62] Y.-H. Lou, Y.-X. Zhu, G.-F. Fan, W. Lei, W.-Z. Lu, and X.-C. Wang, "Design of Ku-band flat Luneburg lens using ceramic 3-D printing," *IEEE Antennas Wireless Propag. Lett.*, vol. 20, no. 2, pp. 234–238, Feb. 2021.
[63] F. Wang, Z. Li, Y. Lou, F. Zeng, M. Hao, W. Lei, X. Wang, X. Wang, G. Fan, and W. Lu, "Stereolithographic additive manufacturing of Luneburg lens using Al_2O_3-based low sintering temperature ceramics for 5G MIMO antenna," *Additive Manuf.*, vol. 47, Nov. 2021, Art. no. 102244.
[64] P. Kadera, J. Lacik, and H. Arthaber, "Effective relative permittivity determination of 3D printed artificial dielectric substrates based on a cross unit cell," *Radioengineering*, vol. 30, no. 4, pp. 595–610, Sep. 2021.
[65] M. Schwentenwein and J. Homa, "Additive manufacturing of dense alumina ceramics," *Int. J. Appl. Ceram. Technol.*, vol. 12, no. 1, pp. 1–7, Jan. 2015.
[66] M. Schwentenwein, P. Chneider, and J. Homa, "Lithography-based ceramic manufacturing: A novel technique for additive manufacturing of high-performance ceramics," *Adv. Sci. Technol.*, vol. 88, pp. 60–64, Oct. 2014.
[67] Lithoz. *3D Printing*. Accessed: Jan. 30, 2022. [Online]. Available: https://www.lithoz.com/
[68] Y. Lou, F. Wang, Z. Li, Z. Zou, G. Fan, X. Wang, W. Lei, and W. Lu, "Fabrication of high-performance $MgTiO_3$–$CaTiO_3$ microwave ceramics through a stereolithography-based 3D printing," *Ceram. Int.*, vol. 46, no. 10, pp. 16979–16986, Jul. 2020.
[69] *Radar Cross Section Handbook*, vol. 2, G. T. Ruck, Ed. New York, NY, USA: Plenum Publishing Corp., 1970.

PETR KADĚRA (Graduate Student Member, IEEE) was born in Čeladná, Czech Republic, in 1994. He received the M.Sc. degree in electronics and communications from the Brno University of Technology, Brno, Czech Republic, in 2018, where he is currently pursuing the Ph.D. degree with the Department of Radio Electronics. In 2020 and 2021, he was a visiting Ph.D. student at TU Darmstadt, Darmstadt, Germany; and the KTH Royal Institute of Technology, Stockholm, Sweden. His current research interests include 3D printing, artificial dielectrics, lens antennas, material characterization, and transformation optics in microwave and millimeter-wave frequencies.

JESÚS SÁNCHEZ-PASTOR (Graduate Student Member, IEEE) received the double master's degrees in telecommunications engineering from the Polytechnic University of Valencia, Spain, and in information and communication engineering from Technische Universität Darmstadt (TU Darmstadt), Germany, in 2020. He is currently pursuing the Ph.D. degree with the Institute of Microwave Engineering and Photonics, TU Darmstadt. His current research interests include chipless RFID applied to indoor localization and sensing, high-Q photonic crystal cavities, and frequency selective surfaces.

HOSSEIN ESKANDARI received the B.Sc. degree in electrical engineering and the M.Sc. and Ph.D. degrees in telecommunication engineering (field and waves) from the Ferdowsi University of Mashhad, Iran, in 2012, 2014, and 2020, respectively. His research interests include transformation-optical design of devices in microwave and photonics, antenna and phased array design, and all-dielectric lens design and fabrication.

TOMÁŠ TYC received the M.Sc. and Ph.D. degrees in theoretical physics from Masaryk University, Brno, in 1996 and 1999, respectively. He obtained the habilitation and the full professorship from Masaryk University, in 2006 and 2009, respectively. He was a Research Fellow or a Visiting Professor with the University of Vienna, in 2000; Macquarie University, Sydney, from 2001 to 2002; the University of Calgary, in 2004; the University of St. Andrews, in 2007 and 2008 and from 2010 to 2012; and the University of Dundee, from 2013 to 2014. He is currently with the Institute of Theoretical Physics and Astrophysics, Masaryk University. He was initially involved in quantum mechanics, quantum optics, and quantum information theory. His research interests include optics, in particular theory of invisible cloaking, transformation optics, and geodesic lenses.

MASOUD SAKAKI received the Ph.D. degree in materials science and engineering, in 2010. He was an Assistant Professor with Malayer University, Iran, from 2010 to 2014; and a Postdoctoral Researcher with Kochi University, Japan, from 2014 to 2019. He is currently a Postdoctoral Researcher with the University of Duisburg–Essen. His main expertises are synthesis, characterization, and sintering of ceramic compounds via different routes. His research interest includes additive manufacturing of ceramics for THz applications.

MARTIN SCHÜßLER received the Dipl.-Ing. and Ph.D. degrees from Technische Universität Darmstadt, Germany, in 1992 and 1998, respectively. He has been a Staff Member with the Institute for Microwave Engineering and Photonics, Technische Universität Darmstadt, since 1998. During his career, he worked in the fields of III–V semiconductor technology, microwave sensors for industrial applications, RFID, and small antennas. His current research interests include microwave biosensors and passive chipless RFID.

ROLF JAKOBY (Member, IEEE) was born in Kinheim, Germany, in 1958. He received the Dipl.-Ing. and Dr.-Ing. degrees in electrical engineering from the University of Siegen, Germany, in 1985 and 1990, respectively. In 1991, he joined the Research Center of Deutsche Telekom, Darmstadt, Germany. Since 1997, he has been a Full Professor with the Technische Universität Darmstadt. He is the Co-Founder of ALCAN Systems GmbH, an author of more than 320 publications, and holds 20 patents. His current research interests include tunable passive microwave devices, beam-steering antennas, chipless RFID sensor tags and biomedical applicators, using metamaterial, ferroelectric, and liquid crystal technologies. He is a member of VDE/ITG and IEEE/MTT/AP societies. He received an award from CCI Siegen for his excellent Ph.D., in 1992; and the ITG-Prize for an excellent publication in the IEEE TRANSACTIONS ON ANTENNAS AND PROPAGATION, in 1997. His group has received 23 awards and prizes for best papers and doctoral dissertations. He was the Chairperson of the EuMC, in 2007, and the GeMiC, in 2011; and was a Treasurer of the EuMW, in 2013 and 2017. He is the Editor-in-Chief of *Frequenz* (De Gruyter).

NIELS BENSON (Member, IEEE) received the Dipl.-Ing. degree in electrical engineering from the University of Stuttgart, in 2004, and the Dr.-Ing. degree in materials science from Technische Universität Darmstadt, in 2009. Since 2008, he has been a Senior Scientist for polymer vision on rollable active matrix displays. In 2010, he joined the University of Duisburg–Essen as the Research Group Leader on thin film photovoltaics and electronics. In 2018, he was appointed as a W1-Professor at the University of Duisburg–Essen on printable materials for signal processing systems. His current research interests include charge carrier transport in disordered semiconductor, passive chipless RFID systems, and additive manufactured ceramic components for sub-mm and mm-wave signal processing applications.

ALEJANDRO JIMÉNEZ-SÁEZ (Member, IEEE) received the double master's degrees (Hons.) in telecommunications engineering from the Polytechnic University of Valencia, Spain, and in electrical engineering from Technische Universität Darmstadt (TU Darmstadt), Germany, in 2017, and the Dr.-Ing. degree *(summa cum laude)* from TU Darmstadt, in 2021. He currently leads the Smart RF Systems-Based on Artificial and Functional Materials Research Group, Institute of Microwave Engineering and Photonics, TU Darmstadt. His current research interests include chipless RFID, high-Q resonators, electromagnetic bandgap structures, liquid crystals, and reconfigurable intelligent surfaces at sub-mm and mm-wave frequencies. He received the Freunde der TU Darmstadt Award for the best dissertation in elektrotechnik und informationstechnik at TU Darmstadt, in 2021.

JAROSLAV LÁČÍK (Member, IEEE) received the M.Sc. and Ph.D. degrees from the Brno University of Technology, Brno, Czech Republic, in 2002 and 2007, respectively. He is currently an Associate Professor with the Brno University of Technology. His research interests include antennas, body-centric wireless communication, computational electromagnetics, and measurement.